AGU ADVANCING EARTH AND SPACE SCIENCE

Geophysical Research Letters®

RESEARCH LETTER
10.1029/2022GL098078

Atmospheric Lunar Tide in the Low Latitude Thermosphere-Ionosphere

Ruth S. Lieberman[1], Brian J. Harding[2], Roderick A. Heelis[3], Nicholas M. Pedatella[4], Jeffrey M. Forbes[5], and Jens Oberheide[6]

[1]NASA Goddard Space Flight Center, Greenbelt, MD, USA, [2]University of California, Berkeley, CA, USA, [3]University of Texas, Dallas, TX, USA, [4]University Corporation for Atmospheric Research, Boulder, CO, USA, [5]University of Colorado, Boulder, CO, USA, [6]Clemson University, Clemson, SC, USA

Abstract We present simultaneous, independent measurements of the atmospheric semidiurnal lunar tide in neutral winds and plasma velocities from NASA's Ionospheric Connection Explorer, and in atomic oxygen 135.6 nm airglow measured by the Global-scale Observations of the Limb and Disk. Westward tidal winds near 115 km at the magnetic equator occur during part of the upward phase of the in-situ plasma drift. Vertical motions associated with the field-aligned plasma velocity occur away from the magnetic equator. The morphology of the lunar tide, and the phasing between the airglow and plasma velocities are consistent with $\mathbf{E} \times \mathbf{B}$ drift as a mechanism for linking neutral wind and plasma perturbations. This work provides the first observational quantification of global-scale E- and F-region coupling through $\mathbf{E} \times \mathbf{B}$ and field-aligned vertical drifts.

Plain Language Summary Tidal winds propagating upward from the neutral atmosphere influence ionospheric dynamo electric fields and vertical plasma drifts. However, these mechanisms have never been fully identified in comprehensive and simultaneous measurements spanning the ionosphere-thermosphere-mesosphere (ITM) system. The atmospheric lunar tide is an effective marker of ITM coupling because it originates at Earth's surface, propagates vertically, and is fully sampled in daytime-only and post-sunset satellite measurements. We utilize measurements from two new NASA missions to track the lunar tide in neutral and plasma velocities, and in an electron density proxy. Our work provides observational confirmation, and quantitative estimates of F-region vertical plasma motions driven by neutral winds and electrodynamical forces.

Key Points:

- The semidiurnal lunar tide is identified in simultaneous, independent measurements of F-region airglow, and neutral and plasma velocities
- Tidal patterns observed in airglow, plasma and neutral motions are consistent with both field-aligned and $\mathbf{E} \times \mathbf{B}$ mechanisms of plasma uplift
- The semidiurnal lunar tide is an effective marker of atmosphere-ionosphere coupling

Correspondence to:
R. S. Lieberman,
ruth.s.lieberman@nasa.gov

Citation:
Lieberman, R. S., Harding, B. J., Heelis, R. A., Pedatella, N. M., Forbes, J. M., & Oberheide, J. (2022). Atmospheric lunar tide in the low latitude thermosphere-ionosphere. *Geophysical Research Letters*, *49*, e2022GL098078. https://doi.org/10.1029/2022GL098078

Received 28 JAN 2022
Accepted 5 MAY 2022

Author Contributions:
Conceptualization: Ruth S. Lieberman, Brian J. Harding, Nicholas M. Pedatella, Jeffrey M. Forbes, Jens Oberheide
Data curation: Nicholas M. Pedatella
Formal analysis: Ruth S. Lieberman
Funding acquisition: Ruth S. Lieberman
Methodology: Ruth S. Lieberman
Project Administration: Ruth S. Lieberman
Resources: Nicholas M. Pedatella
Software: Ruth S. Lieberman
Supervision: Ruth S. Lieberman
Validation: Ruth S. Lieberman
Writing – original draft: Ruth S. Lieberman, Brian J. Harding, Nicholas M. Pedatella, Jeffrey M. Forbes, Jens Oberheide

1. Introduction

Atmospheric lunar tides are global-scale oscillations driven by the gravitational force exerted by the moon (Chapman & Lindzen, 1970), and by tidally-induced motions in the ocean and the solid earth (Vial & Forbes, 1994). Variations in the moon's orbit, along with the motion of the earth relative to the moon give rise to a spectrum of lunitidal frequencies (Siebert, 1961). The most significant of these is the migrating semidiurnal lunar tide (denoted M_2), with a zonal wavenumber of 2 and a period of 12.42 solar hours, or one half of a lunar day. Dynamically, lunar tides are global scale, vertically propagating inertia-gravity waves, whose amplitudes increase with altitude to about 10 m s^{-1} at meteor ablation heights (70–110 km). The predicted vertical wavelength (λ_z) of the classical main M_2 mode is about 150 km (Chapman & Lindzen, 1970).

Early reports of lunar tides in tropical mesospheric and lower thermospheric (MLT) winds were presented by Stening et al. (1997) and Stening et al. (2003). These studies were followed by investigations of M_2 in radar winds at Ascension Island (8°S, 14.4°W) (Sandford & Mitchell, 2007), and the Arctic (Sandford et al., 2006) and Antarctic (Sandford et al., 2007). M_2 maximized between 8 and 11 m s^{-1} during solstice, and exhibited λ_z between 10 and 60 km. Characteristics at ionospheric heights (90–160 km) were historically inferred from signatures in electron drifts and geomagnetic perturbations. Observations from the Jicamarca Radio Observatory (11.95°S, 76.87°W) and the Huancayo Geomagnetic Observatory (12.04°S, 73.82°W) reveal an annual cycle in the lunar geomagnetic field (maximum in January-February, minimum in July-August), a solar local time (SLT) dependence in the M_2 electron drift (Tarpley & Balsley, 1972), and more recently, significant quiet-time day-to-day variability (Eccles et al., 2011).

Global perspectives of M_2 in the MLT have been provided by Zhang and Forbes (2013) for winds, and Paulino et al. (2013) for temperatures. Satellite-derived wind amplitudes exhibited peak values similar to radar-derived

Writing – review & editing: Ruth S. Lieberman, Nicholas M. Pedatella

amplitudes (12 m s^{-1}). Above 100 km, λ_z contracted to 40–50 km (from the predicted value of 150 km). Global M_2 temperature climatologies indicate maximum amplitudes during solstice, with larger values in December (~8 K) than in June.

Global observational studies of the ionospheric lunar tide focused initially on total electron content (TEC) provided by global positioning systems (Pedatella & Forbes, 2010). M_2 maximized in the crests of the equatorial ionization anomaly (EIA, explained in Section 3) during November-February, and between 0900 and 1500 SLT. Subsequently, lunar tides were identified in global measurements of the equatorial electrojet (Lühr et al., 2012; Yamazaki et al., 2017), thermospheric temperature and air density (Forbes et al., 2013), zonal wind (Lieberman et al., 2015), and electron density (Forbes & Zhang, 2019). Interest in the lunar tide intensified when its connection to sudden stratospheric warming (SSW) was established. During SSW events, M_2 enhancements were reported in MLT winds (Chau et al., 2015; Conte et al., 2017), temperatures (Forbes & Zhang, 2012), the equatorial electrojet (Fejer et al., 2010), vertical plasma drifts (Fejer et al., 2011), TEC (Goncharenko et al., 2010), F-region peak height (Pedatella & Maute, 2015), and ionospheric currents (Eccles et al., 2011; Yamazaki et al., 2012). Forbes and Zhang (2012) convincingly argued that one source of M_2 amplification is its proximity (at 12.42 hr) to an atmospheric resonant response that shifts from 12.81 to 12.43 solar hours under SSW conditions.

The lunar tide thus appears to be a powerful agent for coupling the stratosphere to the ionosphere-thermosphere system. Two primary physical mechanisms are attributed: (a). Away from the magnetic equator, M_2 horizontal winds penetrating directly into the thermosphere move plasma along vertically inclined magnetic field lines (**B**) (Forbes & Zhang, 2019; Rishbeth, 1967). (b). Close to the magnetic equator, M_2 horizontal winds perturb E-region dynamo-driven electric fields (**E**) and $\mathbf{E} \times \mathbf{B}$ particle drifts, thus imprinting upon the F-region electron density (Liu & Richmond, 2013; Pedatella et al., 2014). Although elements of these two mechanisms have been detected across disparate case studies and datasets, neither process has ever been tracked in global, independent, and simultaneous measurements of tidally-varying neutral and plasma parameters.

This paper reports the first concurrent observations of M_2 in E- and F-region neutral winds and plasma velocities, and the OI 135.6 nm airglow associated with F-region O^+ recombination. Section 2 describes the datasets, analysis methods, and a proof of concept validated against a whole atmosphere model. Section 3 focuses on a case study during March 2020, when M_2 registered strongly in neutral winds, plasma drifts and OI airglow. These data enable us, for the first time, to track and quantify the neutral and plasma responses associated with a global-scale monochromatic wave. Our results provide constraints for first-principles models that simulate the F-region response to field-aligned tidal winds, and the tidally-perturbed E-region dynamo.

2. Data and Analysis

NASA's Ionospheric Connection explorer (ICON) mission, launched in October 2019, is charged with characterizing low-latitude ionospheric variability, and its sources. The Michelson Interferometer for Global High-Resolution Thermospheric Imaging (MIGHTI) senses line of sight neutral wind speeds from the Doppler shift of the atomic oxygen red (630.0 nm) and green (557.7 nm) lines (Harding et al., 2017). Two identical sensors observe the limb at 45° and 135° relative to the spacecraft velocity vector, allowing determination of the horizontal wind vector between geographic latitudes 12°S and 42°N. For this study we analyzed version 4 of MIGHTI Level 2 vector winds.

The ion velocity meter (IVM) measures the ion velocity vector at the spacecraft altitude (~575 km) (Heelis et al., 2017). Close to the magnetic equator, vertical motions arise primarily through $\mathbf{E} \times \mathbf{B}$ drift associated with dynamo electric fields between 100 and 150 km. ICON was configured so that neutral and ion velocities are regularly sampled along common magnetic field lines. Thus, the mission provides the first direct, one-to-one associations among electrodynamically coupled neutral winds, electric fields, and plasma velocities (Immel et al., 2021). For this study we analyzed version 5 of IVM Level 2 field-aligned and perpendicular ion velocities.

The Global-scale Observations of the Limb and Disk (GOLD), launched in January 2018, is a NASA mission of opportunity hosted on a communications satellite in geostationary orbit. GOLD views the Earth's far ultraviolet airglow emitted between 134 and 162 nm over the Atlantic Ocean and the American continents (Eastes et al., 2020). Daytime temperatures are retrieved from the rotational structure of the N_2 Lyman-Birge-Hopfield (LBH) emission, that emanates from the lower to middle thermosphere (~120–200 km) (Eastes et al., 2017).

GOLD disk temperatures thus represent a column integrated quantity that peaks near 150 km. The most significant nighttime emission observed by GOLD is at 135.6 nm, produced when O^+ ions recombine to an excited state of atomic oxygen (OI). The OI 135.6 emission peaks in the F region where the electron density maximizes (150–200 km). We analyzed version 3 GOLD Level 2 disk temperatures and OI 135.6 brightness.

Observations are compared with the specified dynamics version of the Whole Atmosphere Community Climate Model with thermosphere-ionosphere eXtension (SD-WACCM-X). WACCM-X is a whole atmosphere model that simulates the chemistry, dynamics, physics and electrodynamics between the surface and the upper thermosphere-ionosphere (4.1×10^{-10} hPa, or ~500–700 km depending on solar activity) (Liu et al., 2018). Variability coming from the lower atmosphere is included by constraining the model dynamical fields to the MERRA-2 reanalysis up to 50 km (Smith et al., 2017). Forcing of the M_2 lunar tide is included based on Pedatella et al. (2012). Realistic, time-varying solar and geomagnetic variability are included through parameterizations based on the F10.7 cm solar radio flux and Kp index, respectively (Emery et al., 2012; Heelis et al., 1982; Solomon & Qian, 2005).

M_2 analysis consists of collecting measurements when K_p index is less than 3 (Matzka et al., 2021), filtering the time-averaged and fixed SLT components, binning the residual in lunar local time (LLT), and fitting the 12-hr harmonic. We omit days when the F10.7 cm index (Tapping, 2013) exceeded 2.5 standard deviations of the mean value computed over the averaging interval. We first demonstrate the analysis with GOLD daytime disk temperatures. For each latitude, longitude, and universal time sampled, a 15-day temperature average is removed from the reported value. This multi-day average spans 12 LLTs, but is fixed in SLT (a property illustrated in Figure 1a), thereby filtering the solar tidal as well as slowly-varying features. Temperature residuals are then sorted into hourly LLT bins at each latitude, and fit to a 12-hr harmonic. The uncertainty of the M_2 estimate is determined by iterating the analysis 100 times upon a known tidal field perturbed by random fluctuations scaled by GOLD's measurement uncertainties (50 K for temperature, and 5 Rayleighs for OI emission).

Analysis of M_2 in ICON data is analogous to GOLD, with some important variations. ICON samples 12 lunar hours over 9 consecutive Earth days, as opposed to the 15 days required for GOLD. Therefore, 9-day averages of neutral and plasma velocities are filtered from all point values. Unlike GOLD, however, the SLTs sampled by ICON drift backward in time at the rate of 27 min per day, thus retrograding by 4 hr over the 9-day averaging period (illustrated in Figure 1e). Therefore, a single 9-day average does not fully remove solar tidal components. To mitigate this contamination, we repeat the filtering process for multiple, adjacent 9-day sequences, until 24 solar hours are spanned. At altitudes where MIGHTI samples during daytime and nighttime (90–115 km, and above 200 km), generally four adjacent 9-day sequences are required to sample 24 SLTs. Once this coverage is attained, the filtered data are binned in LLT, and fit to the 12-hr harmonic. The uncertainty of the ICON-based M_2 estimate is determined as for GOLD, using MIGHTI error values of 13 m s^{-1} for individual green line wind retrievals at 108 km, 4.8 m s^{-1} for red line winds at 240 km, and 4.5 m s^{-1} for IVM plasma motions.

Figures 1b and 1f illustrate examples of the analysis method applied to GOLD disk temperatures and MIGHTI zonal winds centered on 15 March 2020. The nominal altitude of GOLD temperatures is 150 km. Their distribution shows a clear 12-hr variation in LLT. The M_2 fit to the temperatures (panel c) is asymmetric about the equator, with an amplitude maximum of 6 K centered at 20°N. The hour of maximum is 0230 LLT in the northern hemisphere, and 0830 LLT in the southern hemisphere. The uncertainty of the M_2 fit at each LLT is 1.6 K. Figure 1d shows a comparison with SD-WACCM-X M_2 temperatures at 150 km, under solar and geomagnetic conditions for March 2020. M_2 is extracted from model temperatures during March 1–31, that have been filtered of the monthly mean SLT average at every point, binned in LLT, and fitted to M_2. The model and the data are qualitatively similar insofar as M_2 is stronger in the northern hemisphere, where their phases agree. However, model amplitudes are weaker by a factor of three, and the data indicate a 180° phase shift near 20°S. Nevertheless, we conclude that our analysis method recovers M_2 in GOLD data with high fidelity.

Figure 1f shows MIGHTI LLT variations of zonal winds at 114 km, computed from data collected between 27 February and 3 April 2020. The M_2 fit is shown in panel 1g, and has an uncertainty of 0.6 m s^{-1} for each LLT. Amplitude maxima of ~6 m s^{-1} appear at the equator and between 5 and 20°N. The hour of maximum occurs at 0300 LLT at the equator, shifting to 0100 LLT at 15°N. M_2 zonal winds in SD-WACCM-X (analyzed identically to the temperatures) are shown in panel 1h. Both patterns show a continuous extension of M_2 between 10°S–20°N. The phase of SD-WACCM-X is nearly constant in latitude, with a maximum at 0300LT. The data, however,

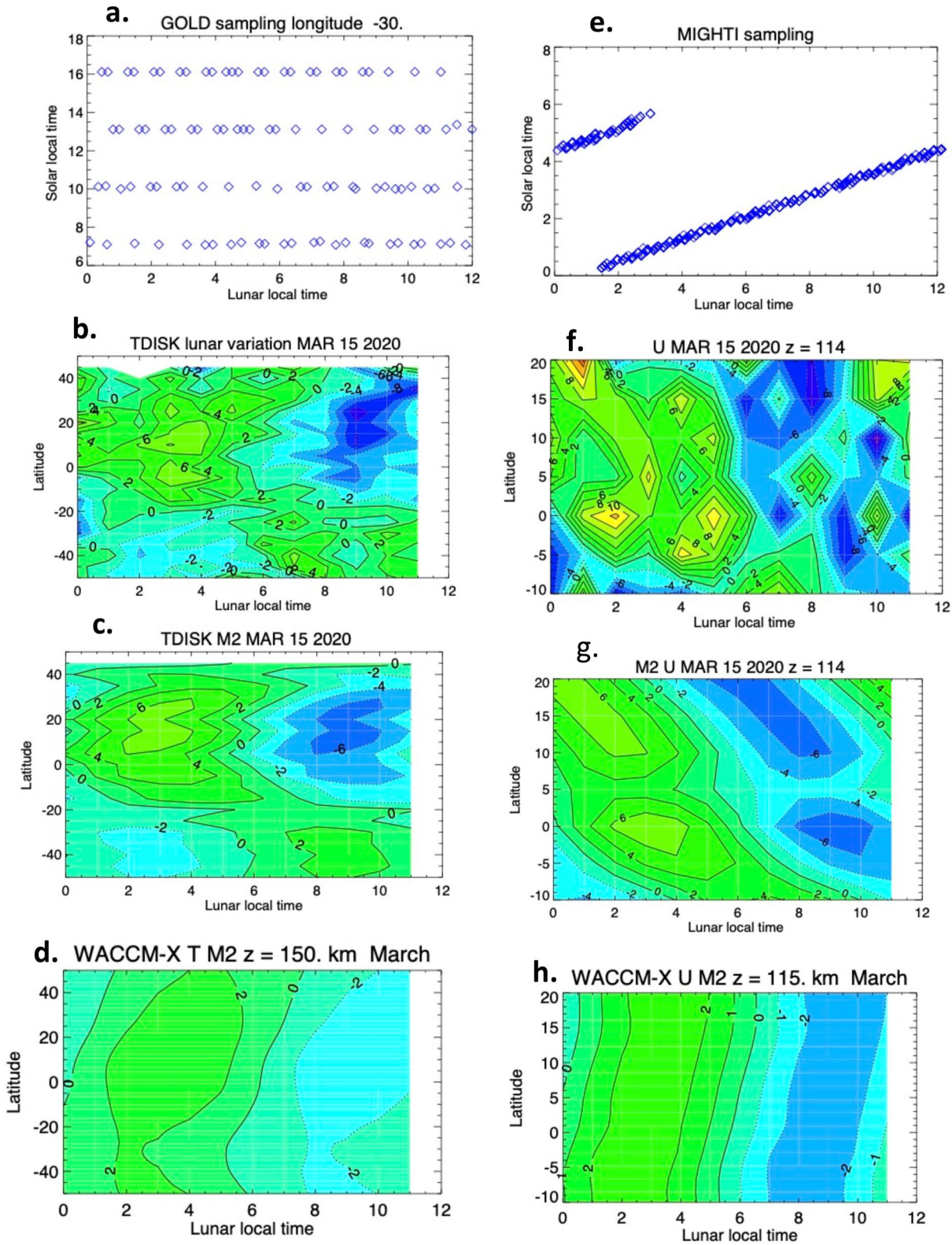

Figure 1. (a) Lunar local time (LLTs) sampled by Global-scale Observations of the Limb and Disk (GOLD) between 0700 and 1600 solar local time during 3–27 March 2020. (b) GOLD temperatures collected during 8–23 March 2020, as a function of LLT (c) M_2 fit to temperatures in (b). d) M_2 fit to SD-WACCM-X March 2020 temperatures at 160 km. (e) LLTs sampled on the ascending portion of ICON's orbit between 27–3 February April 2020. (f) Michelson Interferometer for Global High-Resolution Thermospheric Imaging (MIGHTI) winds sampled at 114 km between 27 February and 3 April 2020, plotted in LLT. (g) M_2 fitted to winds in (f). h) As in d, for SD-WACCM-X zonal winds at 115 km.

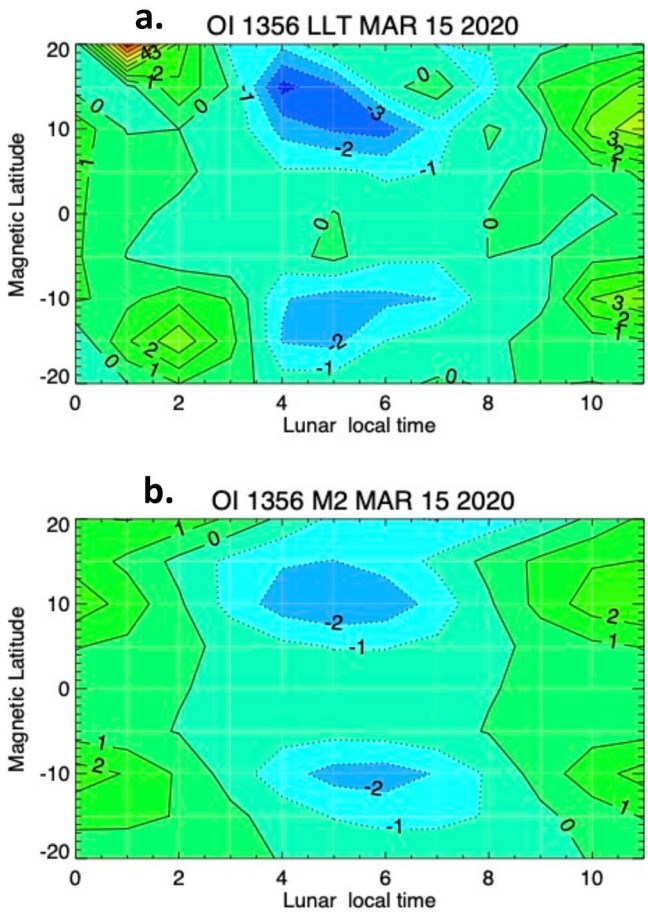

Figure 2. (a) Global-scale Observations of the Limb and Disk atomic oxygen (OI) 135.6 nm emission (in Ra) sampled between 3 and 27 March 2020. (b) M_2 fit to (a).

show a phase retrogression ranging from 0530 LLT at 10°S to 0100 LLT at 15°N. Observed amplitudes exceed the model amplitudes by a factor of three.

We analyzed M_2 in an artificial data set constructed from the 12-and 24-hr solar tides recovered from MIGHTI winds sampled over 24 hr between February 20–10 April 2020. For the wind values shown in Figures 1g and 4a, solar tidal leakage into M_2 (not shown) is roughly 15% of the magnitude between 0 and 10°N, increasing to 20% south of 5°S and north of 15°N. Based on the overall consistency of M_2 morphologies in SD-WACCM-X and ICON, and confinement of solar tide aliasing to 15% at the equatorial latitudes, we conclude that our analysis of ICON winds yields a valid M_2.

3. Lunar Tide in the Ionosphere-Thermosphere

This section presents observations of M_2 during March 2020 in three quantities that are electrodynamically coupled at low latitudes: OI airglow, E-region neutral winds, and plasma velocities. We begin with the analysis OI 135.6 nm brightness in Figure 2. Although the procedure is analogous to that for disk temperatures, brightness is measured over fewer hours per day, therefore requiring 25 consecutive Earth days to sample 12 lunar hours. Thus, we subtract 25-day averages from each data point to remove the time mean and solar tidal features. Figure 2a shows the 135.6 nm nighttime disk brightness (in Rayleighs, or Ra) between 3 and 27 March 2020, plotted in LLT and magnetic latitude. The brightness is highly coherent in latitude, symmetric about the magnetic equator, and shows a clear 12-hr variation. The M_2 fit, shown in Figure 2b, has a maximum amplitude of 2 Ra at 10°S and 10°N, and hour of maximum at 00 LLT. The uncertainty associated with the fitted values is 0.3 R. To place the M_2 retrievals in context, the peak nightly-averaged brightness at ±15° is roughly 6 Ra. We conclude that the M_2 signal in OI 135.6 nm is credible, and significant.

The OI emission is a proxy for plasma density, since its rate of production is proportional to electron and O^+ densities. The latitudinal structuring seen in Figure 2 strongly suggests that M_2 is modulating the nightside EIA. The EIA refers to a region of enhanced ionization that generally peaks near 15°N and 15°S magnetic latitude. This phenomenon results from the daytime E-region electric field, that lofts ionospheric plasma through the $\mathbf{E} \times \mathbf{B}$ mechanism at the magnetic equator. Uplifted particles diffuse along magnetic field lines, drifting poleward and downward (Balan et al., 2018). This so-called "fountain effect" appears as a plasma deficit at the magnetic equator, and as regions of enhanced ion and electron densities typically centered near ±15° in magnetic latitude during geomagnetically quiet conditions (Appleton, 1946; Balan et al., 2018).

Our next steps are to identify elements of the EIA—E-region winds and plasma drifts—concurrent with the OI 135.6 nm emission seen in Figure 2. Figure 3a shows zonal winds at 114 km, computed from MIGHTI winds sampled between 27 February and 3 April 2020, and mapped into LLT versus magnetic latitude. Figure 3b is the projection of Figure 3a into M_2. The highest wind values are about 10 m s^{-1}, observed at the magnetic equator at 0300 LLT. M_2 undergoes nearly 180° phase shifts near 10°S and 15°N. The March M_2 zonal wind pattern in SD-WACCM-X, shown in Figure 3c, is much smoother in latitude, and a factor of four weaker in amplitude at the magnetic equator. However, the hour of maximum ranges from 0200 LLT at 20°S to 0330 LLT at 20°N, with a maximum at 0300 LLT at the magnetic equator that is consistent with the MIGHTI zonal wind.

Horizontal wind motions in the E-region induce charge separation by transporting collisional ions, while electrons gyrate about and translate along **B**. The resultant **E** is oriented upwind, and drives $\mathbf{E} \times \mathbf{B}$ plasma drifts near the magnetic equator. For northward-pointing **B**, upward (downward) drift would result from height-integrated, conductivity-weighted westward (eastward) M_2 zonal winds. Figure 3d shows the vertical component of the IVM in-situ ion velocity perpendicular to local **B**. The 12-hr variation dominates the unfiltered drift. The M_2 fit is shown in Figure 3e. The maximum upward (downward) drift is seen at 1100 LLT at the magnetic equator, two

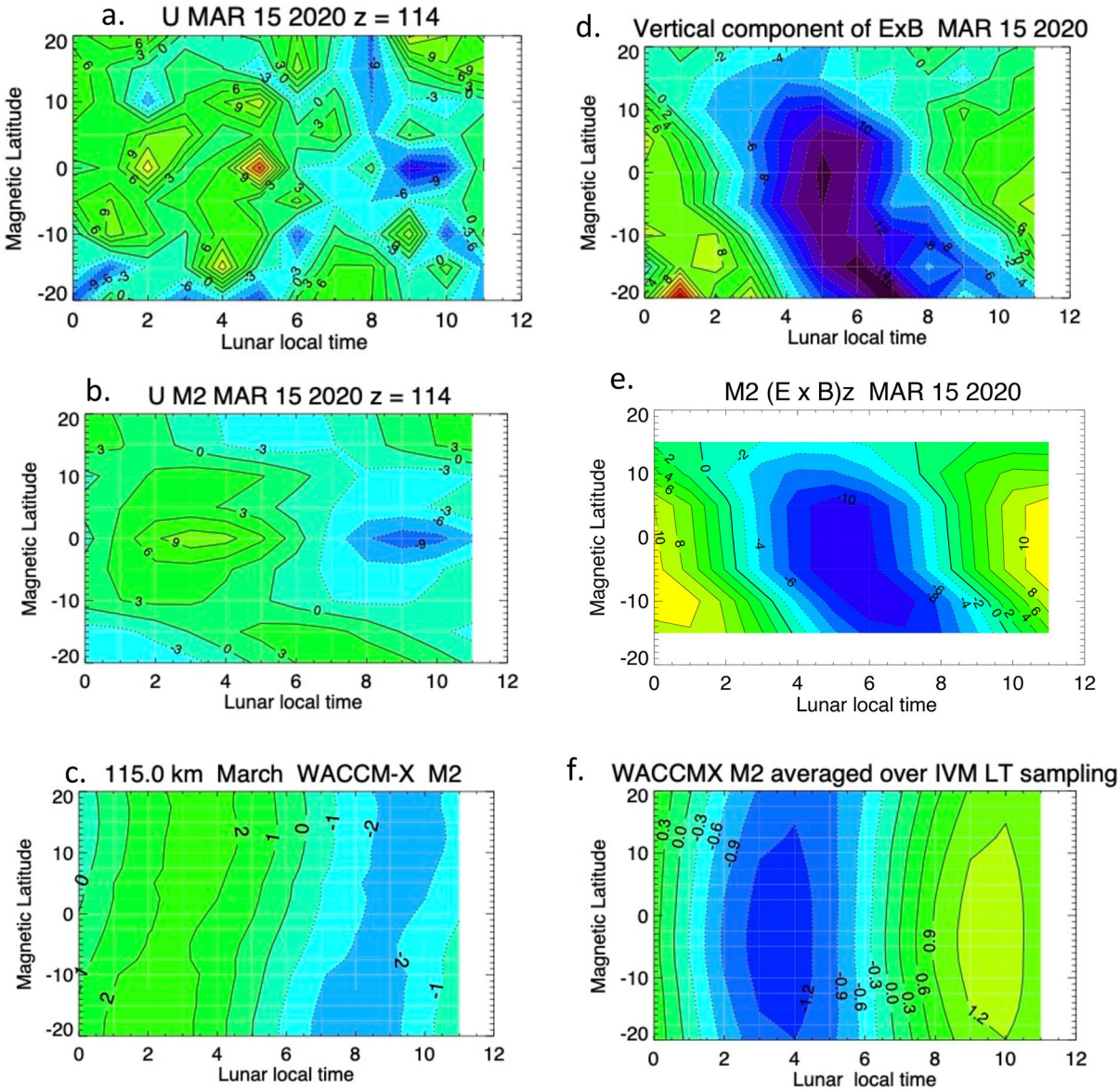

Figure 3. (a) Michelson Interferometer for Global High-Resolution Thermospheric Imaging zonal winds at 114 km between 27 February and 3 April 2020 and mapped to magnetic latitude. (b) M_2 fit to winds in panel (a). c) M_2 in SD-WACCM-X March zonal winds at 114 km, mapped to magnetic latitude. (d) Vertical component of ion velocity meter (IVM) plasma drift perpendicular to local **B**. (e) M_2 fit to drifts in panel (d). (f) M_2 in SD-WACCM-X March vertical drift at 300 km.

hours later than the westward (eastward) E-region M_2 winds. Figure 3f shows the SD-WAACM-X vertical drift near 300 km in March 2020. Like the zonal wind, the model amplitude is substantially weaker than observed. The phase of the upward drift lags the model E-region zonal wind by about 45 min at the magnetic equator.

SD-WACCM-X conforms to the paradigm of an E-region zonal wind being the primary driver of the zonal current and associated $\mathbf{E} \times \mathbf{B}$ drift in the F region. However, the lag observed between the ICON E-region zonal wind and the $\mathbf{E} \times \mathbf{B}$ drift near 600 km is roughly 2 hours. The reason for this excessive phase delay in the data is unclear. Ion velocity meter (IVM) M_2 retrievals are subject to uncertainties due to propagation of measurement error through the fitting process. These have been estimated at only 0.2 m s^{-1}, and do not affect the phase lag. IVM perpendicular drifts are sampled at fewer local times than MIGHTI lower thermospheric winds. However, analysis of MIGHTI winds matched to IVM local time sampling had no effect on the phasing. Aliasing of IVM M_2 analyses by the solar tides has been estimated by sampling diurnal and semidiurnal harmonics in SD-WACCM-X

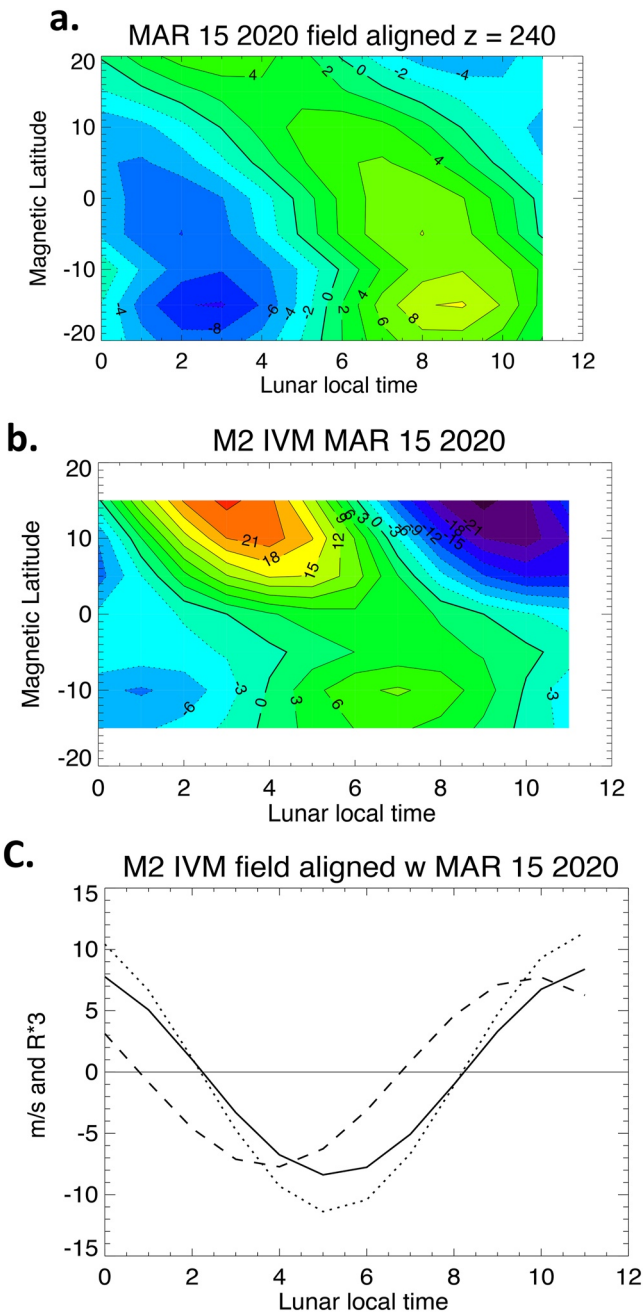

Figure 4. (a) M_2 in Michelson Interferometer for Global High-Resolution Thermospheric Imaging field-aligned winds at 240 km, as a function of magnetic latitude, computed from data between 27 February and 3 April 2020. (b) M_2 component of ion velocity meter (IVM) in-situ plasma drift parallel to local **B**. (c) M_2 in OI emission multiplied by 3 at 10°N (solid curve), $\mathbf{E} \times \mathbf{B}$ vertical drift at the magnetic equator (dotted curve), and the vertical component of field-aligned plasma drift shown in b at 10°N (broken curve).

vertical drift according to IVM, and projecting these into the M_2 fit to $\mathbf{E} \times \mathbf{B}$ drift. At the magnetic equator, the effects of tidal aliasing are minimal, with no influence on the phase.

Thermospheric winds can move F-region plasma along geomagnetic field lines, thereby generating vertical plasma drifts where **B** is vertically inclined (Rishbeth, 2006). Figure 4a shows the M_2 fit to MIGHTI winds parallel to **B** at 240 km. The uncertainty of the fit at each LLT is 0.2 m s^{-1}. The field-aligned component of the horizontal neutral motion is antisymmetric with respect to 10°N magnetic latitude. Amplitude maxima of 10 and 5 m s^{-1} are seen at 15°S and 20°N, respectively.

The corresponding in-situ field-aligned plasma velocity from IVM is shown in Figure 4b. The magnitude of the plasma drift is highly asymmetric about the equator, with northern hemisphere amplitude maxima exceeding their southern hemisphere counterpart by a factor of three. Morphologically, the plasma and neutral wind patterns resemble each other, with key features shifted in LLT. The "saddle point" occurs at 5°S for the field-aligned plasma pattern, compared to 10°N for the neutral wind. At 20°N, the plasma drift and the neutral meridional wind are nearly in phase, while south of the magnetic equator, the plasma drift leads the neutral wind by one hour. The morphological resemblance suggests that the field aligned ion drift is influenced by the neutral wind. However, other processes affect the field-aligned distribution, such as field-aligned gradients in the plasma pressure (Burrell & Heelis, 2012). This force is not currently modeled with SD-WACCM-X electrodynamics, but can be explored further in ionospheric models that include neutral atmosphere forcing.

Finally, Figure 4c shows the relationships among $\boldsymbol{E} \times \boldsymbol{B}$ drift at the magnetic equator, and vertical field-aligned plasma drift and OI 135.6 airglow on the northward flank of the magnetic equator. The vertical $\mathbf{E} \times \mathbf{B}$ drift is in phase with the airglow emission at the magnetic equator. Away from the equator, the vertical projection of the field-aligned drift leads the OI emission by about 1 hour, and is comparable in magnitude to the $\mathbf{E} \times \mathbf{B}$ drift. The close phasing suggests a role for field-aligned drift in the EIA structuring.

4. Summary

The atmospheric lunar tide is an effective marker of global-scale coupling between the lower and upper atmosphere because it originates at Earth's surface, propagates vertically, and is fully sampled in daytime- and post sunset-only satellite measurements. We have identified M_2 in GOLD OI 135.6 nm emission, and in ICON neutral wind profiles and in-situ ion velocities during March 2020. The airglow perturbation has an amplitude of 2 Ra, and the neutral winds and ion drifts have amplitudes of about 10 m s^{-1}. In the positive phase of the airglow, corresponding to O^+ recombination, in-situ vertical ion drift is upward at the magnetic equator. This phasing suggests control of low latitude OI 135.5 emission by $\mathbf{E} \times \mathbf{B}$ plasma uplift at the magnetic equator, and the "fountain effect" on either side of the equator. However, while E-region neutral winds are directed westward over much of the interval when in-situ plasma is lofted at the magnetic equator, the $\mathbf{E} \times \mathbf{B}$ drift lags the zonal wind by 2 hours. The reason for the phase delay could not be determined.

The latitudinal structure of M_2 field-aligned thermospheric wind has some morphological similarities to M2 in-situ field aligned plasma drift. However, the amplitude of the plasma drift is highly asymmetric about the

magnetic equator. The vertical component of the field-aligned plasma drift peaks at 15°N with a value of 10 m s^{-1}, about one hour prior to the OI 135.6 nm emission peak. This relationship suggests a contribution of field-aligned vertical drift to plasma structuring, in addition to the E-region dynamo.

Our findings for M_2 contribute significantly to knowledge of tidal behavior in the thermosphere and ionosphere. We have demonstrated that tidal components with long (>40 km) vertical wavelengths propagate at least to 240 km, and may directly couple the middle atmosphere and the F region. We have quantified the plasma response to the neutral wind-driven dynamo associated with a monochromatic wave. These estimates provide important constraints on thermosphere-ionosphere coupling via tidal processes in whole atmosphere models.

Data Availability Statement

Ionospheric Connection explorer (ICON) data are processed in the ICON Science Data Center at UCB and available at https://icon.ssl.berkeley.edu/Data. Global-scale Observations of the Limb and Disk (GOLD) data are available at the GOLD Science Data Center (http://gold.cs.ucf.edu/search/). F10.7 cm radio flux indices are available at https://lasp.colorado.edu/lisird/data/penticton_radio_flux/. K_p indices are downloaded from https://www.gfz-potsdam.de/en/kp-index/.

Acknowledgments
Ionospheric Connection explorer is supported by NASA's Explorers Program through contracts NNG12FA45C and NNG12FA42I. RSL was supported through the NASA Heliophysics Innovation Fund program. JO acknowledges support through NASA grants 80NSSC19K0258 and 80NSSC20K1353. RSL thanks Drs. Jia Yue and Scott England for helpful discussions, and Dr. Yosuke Yamazaki and an anonymous referee for their incisive reviews.

References

Appleton, E. (1946). Two anomalies in the ionosphere. *Nature*, *157*(3995), 691. https://doi.org/10.1038/157691a0
Balan, N., Liu, L. B., & Le, H. J. (2018). A brief review of equatorial ionization anomaly and ionospheric irregularities. *Earth and Planetary Physics*, *2*(4), 257–275. https://doi.org/10.26464/epp2018025
Burrell, A. G., & Heelis, R. A. (2012). The influence of hemispheric asymmetries on field-aligned ion drifts at the geomagnetic equator. *Geophysical Research Letters*, *39*(19). https://doi.org/10.1029/2012GL053637
Chapman, S., & Lindzen, R. S. (1970). *Atmospheric tides*. Gordon and Breach.
Chau, J. L., Hoffmann, P., Pedatella, N. M., Matthias, V., & Stober, G. (2015). Upper mesospheric lunar tides over middle and high latitudes during sudden stratospheric warming events. *Journal of Geophysical Research*, *120*(4), 3084–3096. https://doi.org/10.1002/2015JA020998
Conte, J. F., Chau, J. L., Stober, G., Pedatella, N., Maute, A., Hoffmann, P., et al. (2017). Climatology of semidiurnal lunar and solar tides at middle and high latitudes: Interhemispheric comparison. *Journal of Geophysical Research*, *122*(7), 7750–7760. https://doi.org/10.1002/2017JA024396
Eastes, R. W., McClintock, W. E., Burns, A. G., Anderson, D. N., Andersson, L., Aryal, S., et al. (2020). Initial observations by the GOLD mission. *Journal of Geophysical Research*, *125*(7). https://doi.org/10.1029/2020JA027823
Eastes, R. W., McClintock, W. E., Burns, A. G., Anderson, D. N., Andersson, L., Codrescu, M., et al. (2017). The Global-Scale Observations of The Limb and Disk (GOLD) mission. *Space Science Reviews*, *212*(1), 383–408. https://doi.org/10.1007/s11214-017-0392-2
Eccles, V., Rice, D. D., Sojka, J. J., Valladares, C. E., Bullett, T., & Chau, J. L. (2011). Lunar atmospheric tidal effects in the plasma drifts observed by the Low-Latitude Ionospheric Sensor Network. *Journal of Geophysical Research*, *116*(A7). https://doi.org/10.1029/2010JA016282
Emery, B. A., Roble, R. G., Ridley, E. C., Richmond, A. D., Knipp, D. J., Crowley, G., & Maeda, S. (2012). *Parameterization of the ion convection and the auroral oval in the NCAR thermospheric general circulation models*. Tech. Rep. Nos. NCAR/TN-491+STR.
Fejer, B. G., Olson, M. E., Chau, J. L., Stolle, C., Lühr, H., Goncharenko, L. P., et al. (2010). Lunar-dependent equatorial ionospheric electrodynamic effects during sudden stratospheric warmings. *Journal of Geophysical Research*, *115*(A8), A00G03. https://doi.org/10.1029/2010JA015273
Fejer, B. G., Tracy, B. D., Olson, M. E., & Chau, J. L. (2011). Enhanced lunar semidiurnal equatorial vertical plasma drifts during sudden stratospheric warmings. *Geophysical Research Letters*, *38*(L21104). https://doi.org/10.1029/2011GL049788
Forbes, J. M., & Zhang, X. (2012). Lunar tide amplification during the January 2009 stratosphere warming event: Observations and theory. *Journal of Geophysical Research*, *117*(A12312). https://doi.org/10.1029/2012JA017963
Forbes, J. M., & Zhang, X. (2019). Lunar tide in the F region ionosphere. *Journal of Geophysical Research*, *124*(9), 7654–7669. https://doi.org/10.1029/2019JA026603
Forbes, J. M., Zhang, X., Bruinsma, S., & Oberheide, J. (2013). Lunar semidiurnal tide in the thermosphere under solar minimum conditions. *Journal of Geophysical Research: Space Physics*, *118*(4), 1788–1801. https://doi.org/10.1029/2012JA017962
Goncharenko, L., Chau, J. L., Liu, H.-L., & Coster, A. J. (2010). Unexpected connections between the stratosphere and ionosphere. *Geophysical Research Letters*, *37*(L10101). https://doi.org/10.1029/2010GL043125
Harding, B. J., Makela, J. J., Englert, C. R., Marr, K. D., Harlander, J. M., England, S. L., & Immel, T. J. (2017). The MIGHTI wind retrieval algorithm: Description and verification. *Space Science Reviews*, *212*(1–2), 585–600. https://doi.org/10.1007/s11214-017-0359-3
Heelis, R. A., Lowell, J. K., & Spiro, R. W. (1982). A model of the high-latitude ionospheric convection pattern. *Journal of Geophysical Research*, *87*(A8), 6339–6345. https://doi.org/10.1029/JA087iA08p06339
Heelis, R. A., Stoneback, R. A., Perdue, M. D., Depew, M., Morgan, W., Mankey, M., et al. (2017). Ion velocity measurements for the ionospheric connections explorer. *Space Science Reviews*, *212*(1–2), 615–629. https://doi.org/10.1007/s11214-017-0383-3
Immel, T. J., Harding, B. J., Heelis, R. A., Maute, A., Forbes, J. M., England, S. L., et al. (2021). Regulation of ionospheric plasma velocities by thermospheric winds. *Nature Geoscience*, *14*(12), 893–898. https://doi.org/10.1038/s41561-021-00848-4
Lieberman, R. S., Fritts, D., Pedatella, N., Doornbos, E., & Ortland, D. A. (2015). Global observations of thermospheric lunar tidal winds. *Journal of Atmospheric and Solar-Terrestrial Physics*, *128*, 126–133. https://doi.org/10.1016/j.jastp.2015.05.019
Liu, H.-L., Bardeen, C. G., Foster, B. T., Lauritzen, P., Liu, J., Lu, G., et al. (2018). Development and validation of the whole atmosphere community climate model with thermosphere and ionosphere extension (WACCM-X 2.0). *Journal of Advances in Modeling Earth Systems*, *10*(2), 381–402. https://doi.org/10.1002/2017MS001232
Liu, H.-L., & Richmond, A. D. (2013). Attribution of ionospheric vertical plasma drift perturbations to large-scale waves and the dependence on solar activity. *Journal of Geophysical Research*, *118*(5), 2452–2465. https://doi.org/10.1002/jgra.50265

Lühr, H., Siddiqui, T. A., & Maus, S. (2012). Global characteristics of the lunar tidal modulation of the equatorial electrojet derived from CHAMP observations. *ANNGEO*, *30*(3), 527–536. https://doi.org/10.5194/angeo-30-527-2012

Matzka, J., Stolle, C., Yamazaki, Y., Bronkalla, O., & Morschhauser, A. (2021). The geomagnetic Kp index # and derived indices of geomagnetic activity. *Space Weather*, *19*(5). https://doi.org/10.1029/2020SW002641

Paulino, A. R., Batista, P. P., & Batista, I. S. (2013). A global view of the atmospheric lunar semidiurnal tide. *Journal of Geophysical Research*, *118*(D12), 13128–13139. https://doi.org/10.1002/2013JD019818

Pedatella, N. M., & Forbes, J. M. (2010). Global structure of the lunar tide in ionospheric total electron content. *Geophysical Research Letters*, *37*(6). https://doi.org/10.1029/2010GL042781

Pedatella, N. M., Liu, H.-L., Richmond, A. D., Wright, A. D., & Amory-Mazaudier, C. (2012). Atmospheric semidiurnal lunar tide climatology simulated by the whole atmosphere community climate model. *Journal of Geophysical Research*, *117*(A06327). https://doi.org/10.1029/2012JA017792

Pedatella, N. M., Liu, H.-L., Sassi, F., Lei, J., Chau, J. L., & Zhang, X. (2014). Ionosphere variability during the 2009 SSW: Influence of the lunar semidiurnal tide and mechanisms producing electron density variability. *Journal of Geophysical Research*, *119*(5), 3828–3843. https://doi.org/10.1002/2014JA019849

Pedatella, N. M., & Maute, A. (2015). Impact of the semidiurnal lunar tide on the midlatitude thermospheric wind and ionosphere during sudden stratosphere warmings. *Journal of Geophysical Research*, *120*(12), 10–740. https://doi.org/10.1002/2015JA021986

Rishbeth, H. (1967). The effect of winds on the ionospheric F-2 peak. *Journal of Atmospheric and Solar-Terrestrial Physics*, *29*(3), 225–238. https://doi.org/10.1016/0021-9169(67)90192-4

Rishbeth, H. (2006). F region links with the lower atmosphere? *Journal of Atmospheric and Solar-Terrestrial Physics*, *68*(3–5), 469–478. https://doi.org/10.1016/j.jastp.2005.03.017

Sandford, D. J., & Mitchell, N. J. (2007). Lunar tides in the Mesosphere over Ascension Island (8° S, 14.4° W). *Annales Geophysicae*, *25*, 9–12. https://doi.org/10.5194/angeo-25-9-2007

Sandford, D. J., Mitchell, N. J., Vincent, R. A., & Murphy, D. J. (2007). The lunar tides in the Antarctic mesosphere and lower thermosphere. *Journal of Atmospheric and Solar-Terrestrial Physics*, *69*(17–18), 2219–2237. https://doi.org/10.1016/j.jastp.2007.04.010

Sandford, D. J., Muller, H. G., & Mitchell, N. J. (2006). Observations of lunar tides in the mesosphere and lower thermosphere at Arctic and middle latitudes. *Atmospheric Chemistry and Physics*, *6*(12), 4117–4127. https://doi.org/10.5194/acp-6-4117-2006

Siebert, M. (1961). Atmospheric tides. *Advances in Geophysics*, *7*, 105–187. https://doi.org/10.1016/s0065-2687(08)60362-3

Smith, A. K., Pedatella, N. M., Marsh, D. R., & Matsuo, T. (2017). On the dynamical control of the mesosphere-lower thermosphere by the lower and middle atmosphere. *Journal of the Atmospheric Sciences*, *74*(3), 993–947. https://doi.org/10.1175/JAS-D-16-0226.1

Solomon, S. C., & Qian, L. (2005). Solar extreme-ultraviolet irradiance for general circulation models. *Journal of Geophysical Research*, *110*(A10306), A10306. https://doi.org/10.1029/2005JA011160

Stening, R. J., Schlapp, D., & Vincent, R. A. (1997). Lunar tides in the mesosphere over Christmas Island (2N,203E). *Journal of Geophysical Research*, *102*(D22), 26239–26245. https://doi.org/10.1029/97jd00898

Stening, R. J., Tsuda, T., & Nakamura, T. (2003). Lunar tidal winds in the upper atmosphere over Jakarta. *Journal of Geophysical Research*, *108*(A5). https://doi.org/10.1029/2002JA009528

Tapping, K. F. (2013). The 10.7 cm solar radio flux (f10. 7). *Space Weather*, *11*(7), 394–406. https://doi.org/10.1002/swe.20064

Tarpley, J. D., & Balsley, B. B. (1972). Lunar variations in the Peruvian electrojet. *Journal of Geophysical Research*, *77*(10), 1951–1960. https://doi.org/10.1029/JA077i010p01951

Vial, F., & Forbes, J. M. (1994). Monthly simulations of the lunar semi-diurnal tide. *Journal of Atmospheric and Terrestrial Physics*, *56*(12), 1691–1607. https://doi.org/10.1016/0021-9169(94)90089-2

Yamazaki, Y., Richmond, A. D., & Yumoto, K. (2012). Stratospheric warmings and the geomagnetic lunar tide: 1958–2007. *Journal of Geophysical Research*, *117*(A04301). https://doi.org/10.1029/2012JA017514

Yamazaki, Y., Stolle, C., Matzka, J., Siddiqui, T. A., Lühr, H., & Alken, P. T. (2017). Longitudinal variation of the lunar tide in the equatorial electrojet. *Journal of Geophysical Research*, *119*(122), 12445–12463. https://doi.org/10.1002/2017JA024601

Zhang, J. T., & Forbes, J. M. (2013). Lunar tidal winds between 80 and 110 km from UARS/HRDI wind measurements. *Journal of Geophysical Research*, *118*(8), 5296–5304. https://doi.org/10.1002/jgra.50420